Abstract

Natural frequencies, mode shapes and modal damping values are the most important parameters to describe the noise and vibration behaviour of a mechanical system. For rotating machinery, however, the directivity of the propagation wave of each mode should also be taken into account. For rotating systems, this directivity can be determined by complex modal testing. In this paper, a rolling tire is represented as a flexible ring model. The limitation of application of the complex modal testing which requires two directional measurements at a certain point, which is difficult to measure in practice, has been overcome through a modified complex modal testing which requires only one directional measurements at any two points. The technique is described in detail and applied to both a numerical example and to an experimental data set of a real rotating tire.

Keywords: tire dynamics, rotating tire analysis, forward and backward waves, complex modal testing

1 Introduction

The dynamic characteristics of rolling tires have been widely studied in literature by looking at modes and propagating waves [1-3]. Next to the natural frequencies and the damping values, the directivity of the propagation wave of each complex mode (forward and backward wave) is an important parameter for the understanding of the dynamic characteristics of rolling tires. Furthermore, an accurate estimation of the complex mode shape itself is also of great importance [4]. However, the experimental setup needed to identify the mode shapes using conventional modal testing approaches is quite complex and expensive as many points should be measured on the rotating object [1, 2]. For this reason, Lee [5-7] introduced a complex modal testing (CMT) approach for rotating machinery, which makes it possible to estimate the directivity of each wave with only two responses measured at different points and two forces applied at different locations.

The equation of motion for the rotating system is composed of two directions (e.g. for the rotor/bearing system it is described in the Y and Z direction and for the flexible ring model it is described in the radial and circumferential direction). These two directional vibration measurements at a certain point are used in the conventional CMT technique. In current experimental setup of a rotating tire, it is very difficult

to measure the both directional responses (radial and circumferential direction) at a certain point. Therefore, the conventional CMT and the modified CMT that is proposed in this paper can be classified by following explanations. The modified CMT technique, which uses only one directional measurement measured at any two points (in this research the radial direction is used), is introduced with the flexible rotating ring model to get same results to the conventional CMT. And to introduce in a simplified manner, the conventional CMT is developed for estimating the directivity of each wave as well as the degree of anisotropy or asymmetric of rotors by using directional frequency response function (dFRF). In this technique, the dFRF is identified with two directional vibration measurements, which compose the equation of motion of a rotor/bearing system in a Cartesian coordinate, at one position. The proposed modified complex modal testing in this study is developed based on a rotating flexible ring model. In the modified technique, the dFRFs are composed of two vibrational measurements in radial direction measured at two different positions and these are used to confirm the directivity of each wave by the difference of magnitudes between the results in the positive and negative frequency regions of the dFRFs

In fact there are several limitations on analysing dynamic behaviour of a rotating tire with the flexible ring mode as introduced in Ref. [8]. For instance, a rolling tire is deformed by vehicle's weight during driving condition [3]. The proposed ring model, however, has always a circular configuration during rotating condition, in addition, tire includes bending mode in axial direction but ring model cannot take this into account [4]. Despite of these limitations, the reason of adopting the flexible ring model is that it is easy to confirm and to estimate the rotational effects (forward and backward wave) in the analytic FRF result. And this study does not focus on investigation of dynamic changes of a rolling tire by loading and rotating conditions but development of a method to estimate the rotational effects. In addition, it is observed that the estimated rotational effects confirmed by the proposed method are in well agreement with the confirmed results in experimental measurement within interesting frequency region. Hence, it can be concluded that the introduced flexible ring model is effective to analyse rotational effect of a tire.

In the current paper, the conventional CMT theory will be briefly introduced and two measurement

conditions will also be introduced to estimate the directivity of each wave with confidence for the modified CMT technique. And the approach with these conditions will be applied on the case of a rotating tire. First the approach is applied on the numerical case of a tire ring model [9] and afterwards on measurements on a real rotating tire.

2 Complex Modal Testing [5]

2.1 Directional frequency response function

The equation of motion of an isotropic rotor/bearing system under complex force excitation can be written as

$$\mathbf{M}_c \ddot{\mathbf{p}} + \mathbf{C}_c \dot{\mathbf{p}} + \mathbf{K}_c \mathbf{p} = \mathbf{g} \tag{1}$$

with

$$\mathbf{M}_c = \mathbf{M}_1 - j\mathbf{M}_2,\ \mathbf{C}_c = \mathbf{C}_1 - j\mathbf{C}_2,\ \mathbf{K}_c = \mathbf{K}_1 - j\mathbf{K}_2$$
$$\mathbf{M}_1 = \mathbf{M}_{yy} = \mathbf{M}_{zz},\ \mathbf{C}_1 = \mathbf{C}_{yy} = \mathbf{C}_{zz},\ \mathbf{K}_1 = \mathbf{K}_{yy} = \mathbf{K}_{zz}$$
$$\mathbf{M}_2 = \mathbf{M}_{yz} = -\mathbf{M}_{zy},\ \mathbf{C}_2 = \mathbf{C}_{yz} = -\mathbf{C}_{zy},\ \mathbf{K}_2 = \mathbf{K}_{yz} = -\mathbf{K}_{zy}$$

and

$$\mathbf{p} = \mathbf{y} + j\mathbf{z},\ \mathbf{g} = \mathbf{f}_y + j\mathbf{f}_z$$

In eq. (1), vector **p** and **g** represent the complex response vector and the complex force vector which are composed of displacement vectors and external force vectors in *y* and *z* direction, with *y* and *z* describing the plane perpendicular to the axis of rotation, and the size of each vector is $N \times 1$. In addition, subscript *c* represents complex matrices that are composed of complex values. And the size of $\mathbf{M}_c$, $\mathbf{C}_c$ and $\mathbf{K}_c$ is $N \times N$ and the equation can be transformed into a state space form

$$\mathbf{A}_c \dot{\mathbf{w}}_c + \mathbf{B}_c \mathbf{w}_c = \mathbf{F}_c \tag{2}$$

with

$$\mathbf{A}_c = \begin{bmatrix} \mathbf{0} & \mathbf{M}_c \\ \mathbf{M}_c & \mathbf{C}_c \end{bmatrix},\ \mathbf{B}_c = \begin{bmatrix} -\mathbf{M}_c & \mathbf{0} \\ \mathbf{0} & \mathbf{K}_c \end{bmatrix},\ \mathbf{w}_c = \begin{Bmatrix} \dot{\mathbf{p}} \\ \mathbf{p} \end{Bmatrix} \text{ and } \mathbf{F}_c = \begin{Bmatrix} \mathbf{0} \\ \mathbf{g} \end{Bmatrix}$$

The size of the state matrices $\mathbf{A}_c$ and $\mathbf{B}_c$, in eq. (2), is $2N \times 2N$ and these are composed of complex values and are non-symmetric matrices. The size of the state response vector $\mathbf{w}_c$ and the state force vector $\mathbf{F}_c$ is $2N \times 1$. If the eigenvalue problem of eq. (2) is solved with the assumption that $\mathbf{F}_c$ is

equal to **0**, then the eigenvectors and adjoint eigenvectors can be obtained, and the bi-orthogonal property can be satisfied as follows

$$\begin{aligned} \mathbf{l}_{cj}^{H}\,\mathbf{A}_c\,\mathbf{r}_{ci} &= \delta_{ji} \\ \mathbf{l}_{cj}^{H}\,\mathbf{B}_c\,\mathbf{r}_{ci} &= -\lambda_i\,\delta_{ji} \end{aligned} \tag{3}$$

In eq. (3), the vectors $\mathbf{r_c}$ and $\mathbf{l_c}$ represent eigenvectors (right eigenvectors) and adjoint eigenvectors (left eigenvectors), respectively, and λ represents the eigenvalues of the system, which are expressed by complex values. The real terms of λ imply energy dissipation and the imaginary terms of λ refer to the resonance frequencies of the system. Here, positive (+) resonance frequencies represent propagating directivity of the wave in forward direction, while negative (-) resonance frequencies represent propagating in backward direction with respect to the rotating direction of the system. In eq. (3), δ_{ij} represents the Kronecker delta function, which is defined as 1, when the index $i = j$, and as 0 otherwise. The superscript H indicates the Hermitian matrix. The eigenvectors and adjoint eigenvectors are composed as

$$\mathbf{r}_{ci} = \begin{Bmatrix} \lambda\,\boldsymbol{\varphi}_c \\ \boldsymbol{\varphi}_c \end{Bmatrix}_i \,,\; \mathbf{l}_{cj} = \begin{Bmatrix} \bar{\lambda}\,\boldsymbol{\psi}_c \\ \boldsymbol{\psi}_c \end{Bmatrix}_j \tag{4}$$

Here, the bar represents the complex conjugate. The $\boldsymbol{\varphi}_c$ and $\boldsymbol{\psi}_c$ are the modal vector and adjoint modal vector of the eq. (1) and the modal vectors can be used to express the complex displacement vector **p**.

$$\mathbf{p}(t) = \sum_{n=1}^{N} \sum_{i=F,B}{}^{i} \left\{ \boldsymbol{\varphi}_c\,\eta_c(t) \right\}_n \tag{5}$$

In eq. (5), η_c represents the general coordinate of the complex displacement vector **p** and the index i stands for each propagating direction where, F is the forward and B is the backward wave component of each resulting complex mode. Combining eq. (5) and (1), the relation between the complex force and the complex response is obtained in frequency domain (eq. (6)) and the elements of the directional frequency response function (dFRF) are represented in eq. (7).

$$\mathbf{P}(j\omega) = \mathbf{H}_{pg}(j\omega)\mathbf{G}(j\omega) \tag{6}$$

$$\mathbf{H}_{pg}(j\omega) = \sum_{n=1}^{N} \sum_{i=F,B}{}^{i} \left\{ \frac{\boldsymbol{\varphi}_c\,\boldsymbol{\psi}_c^{H}}{j\omega - \lambda} \right\}_n \tag{7}$$

Note that the dFRFs in eq. (7) do not have a conjugate part (i.e. each wave is represented by first order

basis not second order basis) which ensures that the forward wave, which is represented by a positive frequency, is only observed in the positive frequency region and the backward wave, which is represented by a negative frequency, is only observed in the negative frequency region. Therefore, dFRF analysis of rotating systems makes it possible to estimate the propagating directivity of each wave when the dFRFs are investigated in both frequency regions (positive and negative).

3 Modified Complex Modal Testing for a flexible ring

3.1 Transfer function of a rotating flexible ring in global coordinates

In previous works [9-11], a ring model has been used to analyse the dynamic characteristics of tires. The ring is represented in cylindrical coordinates and two reference systems can be used to express its dynamic behaviour. One is a rotating reference which is a local coordinate system. The other one is a fixed reference which is a global coordinate system. In the presented research work, laser Doppler vibrometer is adopted for gaining vibration information of the tire vibration pattern. Therefore, the global coordinate system is used to analyse the dynamic behaviour. Fig. 1 shows the configuration of the rotating flexible ring and its two coordinate systems (global and local).

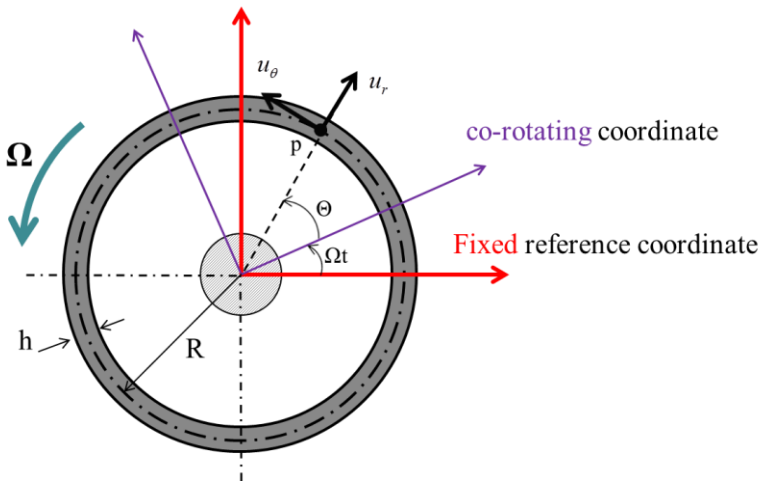

Fig. 1 Global and local coordinates of a rotating flexible ring.

The equation of motion of a rotating ring considering damping in global coordinates is as follows [9, 12]

$$\mathbf{M}\ddot{\mathbf{u}}(\theta,t) + \mathbf{C}\dot{\mathbf{u}}(\theta,t) + \mathbf{K}\mathbf{u}(\theta,t) = \mathbf{q}(\theta,t) \tag{8}$$

with

$$\mathbf{M} = \begin{bmatrix} \rho A & 0 \\ 0 & \rho A \end{bmatrix} \tag{9-1}$$

$$\mathbf{C} = \rho A \begin{bmatrix} \lambda + j2n\Omega & -2\Omega \\ 2\Omega & \lambda + j2n\Omega \end{bmatrix} \tag{9-2}$$

$$\mathbf{K} = \begin{bmatrix} \left(\frac{EI\,n^4}{R^4} + \frac{EA}{R^2} - \rho A\left(jn\Omega\lambda - \Omega^2 - n^2\Omega^2 \right) \right) & j\left(\frac{EIn^3}{R^4} + \frac{nEA}{R^2} - 2n\Omega^2 \right) \\ -j\left(\frac{EIn^3}{R^4} + \frac{nEA}{R^2} - 2n\Omega^2 \right) & \left(\frac{EI\,n^4}{R^4} + \frac{EA}{R^2} - \rho A\left(jn\Omega\lambda - \Omega^2 - n^2\Omega^2 \right) \right) \end{bmatrix} \tag{9-3}$$

$$\mathbf{u} = \begin{Bmatrix} u_r \\ u_\theta \end{Bmatrix}, \ \mathbf{q} = \begin{Bmatrix} q_r \\ q_\theta \end{Bmatrix} \tag{9-4}$$

In eq. (8), **M**, **C** and **K** represent the mass, damping (with gyroscopic terms) and stiffness matrices, respectively, while, the vectors **u** and **q** represent displacements and external forces in radial and circumferential directions, respectively. The size of each matrix is 2×2 and the detailed description of these matrices and vectors are shown in eq. (9). In eq. (9), ρ is the material density, A is the cross sectional area, λ is the internal damping, Ω is the rotational speed, E is the Young's modulus and I is the moment of inertia. The equation shows that the mass matrix is diagonal, while, the damping and stiffness matrices are skew-symmetric matrices which are composed of complex values. In eq. (9-4), u_r and u_Θ represent the radial and circumferential displacement for n^{th} mode, receptively, and these are function of time and spatial domain.

$$u_r(\theta,t) = U_r e^{j(n\theta+\omega t)}, \ u_\theta(\theta,t) = U_\theta e^{j(n\theta+\omega t)} \tag{10}$$

The equation of motion (eq. (8)) can be represented in state space as follows

$$\mathbf{A}\dot{\mathbf{p}} + \mathbf{B}\mathbf{p} = \mathbf{f} \tag{11}$$

with

$$\mathbf{A} = e^{jn\theta}\begin{bmatrix} \mathbf{0} & \mathbf{M} \\ \mathbf{M} & \mathbf{C} \end{bmatrix}, \ \mathbf{B} = e^{jn\theta}\begin{bmatrix} \mathbf{-M} & \mathbf{0} \\ \mathbf{0} & \mathbf{K} \end{bmatrix}, \ \mathbf{p}(t) = \begin{Bmatrix} \dot{\mathbf{u}}(t) \\ \mathbf{u}(t) \end{Bmatrix} \text{ and } \mathbf{f}(t) = \begin{Bmatrix} \mathbf{0} \\ \mathbf{q}(t) \end{Bmatrix}$$

In the previous sections, matrices **A** and **B** were only composed of system properties, however, in this case (rotating tire ring model), the matrices are composed of complex values and their size is 4×4 and they include the space term which is shown in eq. (10). Therefore, the response vector **p** is only a

function of time. If the vector **f** is put to zero and the eigenvalue problems are solved, then, both eigenvectors and adjoint eigenvectors can be obtained; these eigenvectors satisfy the bi-orthogonal property.

$$\begin{aligned} \mathbf{l}_j^T \mathbf{A} \mathbf{r}_i &= \delta_{ji} \\ \mathbf{l}_j^T \mathbf{B} \mathbf{r}_i &= -\lambda_i \delta_{ji} \quad i, j = \pm 1, \pm 2, ..., \pm N \end{aligned} \tag{12}$$

Here, the superscript T represents the transpose matrix. And the eigenvectors and the adjoint eigenvectors are made up of the combination of modal vectors.

$$\mathbf{r}_i = e^{jn\theta} \begin{Bmatrix} \lambda \boldsymbol{\varphi} \\ \boldsymbol{\varphi} \end{Bmatrix}_i , \mathbf{l}_j = e^{jn\theta} \begin{Bmatrix} \bar{\lambda} \boldsymbol{\psi} \\ \boldsymbol{\psi} \end{Bmatrix}_j \tag{13}$$

The space term ($e^{jn\theta}$) is included in the eigenvectors and the adjoint eigenvectors because the term is multiplied to the matrices **A** and **B** as a scalar. Therefore, the vectors **r** and **l** are dependent of space whereas the modal vectors **φ** and the adjoint modal vectors **Ψ** are the unique properties of the system, which are space independent. Here, the modal vectors are composed of radial and circumferential directional elements (φ_r, φ_Θ and Ψ_r, Ψ_Θ). In order to get the FRF, the state vector **p** can be represented as follows

$$\mathbf{p} = \mathbf{R}\boldsymbol{\eta} \tag{14}$$

Here, **R** indicates the matrix of eigenvectors and **η** indicates the vector of general coordinates. Substituting eq. (14) into eq. (11) and multiplying $\mathbf{L}^H$ (the matrix of adjoint eigenvectors) to the left hand of both sides, one can obtain

$$\left(s\mathbf{I} - \boldsymbol{\lambda}_\mathbf{n}\right)\boldsymbol{\eta} = \mathbf{L}^\mathbf{H}\mathbf{f} \tag{15}$$

In eq. (15) 's' indicates Laplace domain, **I** indicates the identity matrix of size 4×4, $\boldsymbol{\lambda}_\mathbf{n}$ is a diagonal matrix composed of eigenvalues. Pre-multiplying the inverse of $\left(s\mathbf{I} - \boldsymbol{\lambda}_\mathbf{n}\right)$ to both sides of the equation gives an equation having vector **η** alone on the left hand side. One can obtain the result (eq. (16)) after multiplying matrix **R** to both sides of the resulting equation.

$$\mathbf{p}(\theta, s) = \mathbf{R}\left(s\mathbf{I} - \boldsymbol{\lambda}_\mathbf{n}\right)^{-1}\mathbf{L}^\mathbf{H}\mathbf{f}(s) \tag{16}$$

Eq. (16) can be expressed in summation form.

$$\mathbf{p}(\theta, s) = \sum_{n=-N;n\neq0}^{N} \sum_{i=F,B} \left\{ \frac{\mathbf{r}_\mathbf{n}\mathbf{l}_\mathbf{n}^\mathbf{H}}{(s - \lambda_n)} \right\}^i \mathbf{f}(s) = \sum_{n=1}^{N} \sum_{i=F,B} \left\{ \frac{\mathbf{r}_\mathbf{n}\mathbf{l}_\mathbf{n}^\mathbf{H}}{(s - \lambda_n)} + \frac{\bar{\mathbf{r}}_\mathbf{n}\mathbf{l}_\mathbf{n}^T}{(s - \bar{\lambda}_n)} \right\}^i \mathbf{f}(s) \tag{172}$$

Even though the system matrices for n^{th} mode **A** and **B** have size of 4×4, if one takes into account N numbers of mode, then the size of these system matrices can be considered as $4N\times4N$ likewise the rotating system; therefore, the response of the ring should be expressed by $4N$ bases functions, as can be deduced from eq. (17) ($2N$ ($-N$ to N) $\times2$ (forward, backward)). In eq. (11), the displacement vector **u** and the external force vector **q** are located in below half of the response state vector **p** and the force state vector **f**, respectively. Therefore, not every element in matrix eq. (17) needs to be considered. It is only necessary to consider the lower part of the eigenvectors and the adjoint eigenvectors to express vector **u**.

$$\mathbf{u}(\theta,s)= \sum_{n=1}^{N}\sum_{i=F,B}\left\{\frac{B\boldsymbol{\varphi}_{\mathbf{n}}\boldsymbol{\psi}_{\mathbf{n}}^{\mathbf{H}}}{\left(s-\lambda_n\right)}+\frac{\bar{B}\bar{\boldsymbol{\varphi}}_{\mathbf{n}}\boldsymbol{\psi}_{\mathbf{n}}^{\mathbf{T}}}{\left(s-\bar{\lambda}_n\right)}\right\}^{i}\mathbf{q}(s) \tag{18}$$

where $B=e^{jn\left(\theta_s-\theta_f\right)}$

Because both the eigenvectors and adjoint eigenvectors include the space information (θ) as shown in eq. (13), it is also included in eq. (18). Here, the location of measurement is indicated by subscript s and the location of the force by subscript f. The scalar B stands for the phase delay which is determined by the locations of the measurement and the force. One can confirm that the principle of reciprocity [13] does not hold in the case of flexible rotating ring since the phase in the scalar B is changed when the two locations (measurement and force) are switched. The equation can be transformed into the frequency domain by substituting s by $j\omega$ and representing the result in matrix form.

$$\mathbf{U}(\theta,j\omega)=\mathbf{H}(\theta,j\omega)\mathbf{Q}(\theta) \text{ or } \begin{Bmatrix}\mathbf{U}_r(\theta,j\omega)\\ \mathbf{U}_\theta(\theta,j\omega)\end{Bmatrix}=\begin{bmatrix}\mathbf{H}_{rr}(\theta,j\omega) & \mathbf{H}_{r\theta}(\theta,j\omega)\\ \mathbf{H}_{\theta r}(\theta,j\omega) & \mathbf{H}_{\theta\theta}(\theta,j\omega)\end{bmatrix}\begin{Bmatrix}\mathbf{Q}_r(j\omega)\\ \mathbf{Q}_\theta(j\omega)\end{Bmatrix} \tag{19}$$

Eq. (19) shows the frequency response matrix (FRM) in which every FRF related to each direction is shown. The element for the radial displacement and the radial force in the FRM is

$$\mathbf{H}_{rr}(\theta,j\omega)=\sum_{n=1}^{N}\sum_{i=F,B}^{i}\left\{\frac{B\boldsymbol{\varphi}_r\boldsymbol{\psi}_r^{H}}{j\omega-\lambda}+\frac{\bar{B}\bar{\boldsymbol{\varphi}}_r\boldsymbol{\psi}_r^{T}}{j\omega-\bar{\lambda}}\right\}_n \tag{20}$$

From eq. (18) and (20), the FRF of a rotating ring follows with the following relation

$$\mathbf{H}_{ik}(-j\omega)=\bar{\mathbf{H}}_{ik}(j\omega),\ i,k=r,\theta \tag{21}$$

In other words, if a FRF is investigated in both positive and negative frequency region, the magnitude in the negative frequency is just the replica of the result in the positive frequency; therefore, it is

impossible to estimate the information of the propagating directivity of each wave with a general FRF similar to the rotating system.

The CMT [5] was introduced for the lumped element system (rotor/bearing). In this system it is possible to measure the two directional (y, z) responses and forces in a Cartesian coordinate to comprise the complex response and force. However, in order to apply the CMT to a flexible ring model, it is required that the radial and circumferential displacement and force are directional elements in the equation of motion. In real experimental configurations of a rolling tire, the circumferential displacement and force are impossible or at least very difficult to measure with current technology (a detailed explanation of the experimental configuration is given in section 5). Therefore, in this research, two vibration measurements only in radial direction, which are measured at different locations, and the radial forces applied at that time (the force always applied at the same position) are used to comprise the complex response and the complex force,

$$p = u_1 + j u_2 \ , \ g = f_r + j f_r \tag{22}$$

Here, u_1 and u_2 are the radial displacements measured at different position (i.e. $\Theta_s = \Theta_1$ and Θ_2), under the assumption that the force is applied with the same magnitude at the same position in every experiment, f_r indicates the applied radial force. Eq. (22) can be used to obtain the following results.

$$\begin{aligned}
2\mathbf{H}_{pg}(j\omega) &= \frac{P}{G} = \mathbf{H}_1 + \mathbf{H}_2 - j(\mathbf{H}_1 - \mathbf{H}_2) \\
2\mathbf{H}_{p\hat{g}}(j\omega) &= \frac{P}{\hat{G}} = \mathbf{H}_1 - \mathbf{H}_2 + j(\mathbf{H}_1 - \mathbf{H}_2) \\
2\mathbf{H}_{\hat{p}g}(j\omega) &= \frac{\hat{P}}{G} = \mathbf{H}_1 - \mathbf{H}_2 - j(\mathbf{H}_1 + \mathbf{H}_2) \\
2\mathbf{H}_{\hat{p}\hat{g}}(j\omega) &= \frac{\hat{P}}{\hat{G}} = \mathbf{H}_1 + \mathbf{H}_2 + j(\mathbf{H}_1 - \mathbf{H}_2)
\end{aligned} \quad \text{where} \quad \mathbf{H}_1 = \frac{U_1}{F_r}, \ \mathbf{H}_2 = \frac{U_2}{F_r} \tag{23}$$

In eq. (23), P and G are transformations of p and g into the frequency domain and $\hat{P}$ and $\hat{G}$ are transformations of the complex conjugate of p and g into the frequency domain. $\mathbf{H}_1$ and $\mathbf{H}_2$ indicate the FRFs in terms of the location of measurement at Θ_1 and Θ_2. In other words, it is confirmed that the two sided dFRFs show different magnitudes between the negative frequency result and the positive frequency result and it can be also expected that the directivity of each wave can be estimated from this. Detailed understanding for the dFRFs in eq. (23) is conducted in the next section.

3.2 Directional frequency response function

Introduced in the previous section, the directional FRFs obtained by the radial displacement measured at two positions and radial force applied at one position cannot be analysed by the equation of motion in the same way as was done in section 2.1 because the equation of motion of a rotating ring is coupled (radial and circumferential direction) due to Coriolis effects whereas the values in eq. (23) only consist of radial information. Therefore, in this research, each magnitude of a directional FRF at a resonance frequency ($j\omega_n$) and at the opposite frequency ($-j\omega_n$) investigated. Through this, the propagating directivity of the each wave is estimated. In eq. (23), $\mathbf{H}_{\hat{p}\hat{g}}$ can be expressed as

$$\mathbf{H}_{\hat{p}\hat{g}}(j\omega) = \left\{\mathbf{H}_1 + \mathbf{H}_2 + j(\mathbf{H}_1 - \mathbf{H}_2)\right\}/2 = \mathbf{H}_2\left\{K(1+j)+(1-j)\right\}/2$$
$$\text{where } K(j\omega) = \frac{H_1(j\omega)}{H_2(j\omega)} = a + jb \tag{24}$$

Here, K indicates the ratio of $\mathbf{H}_1$ and $\mathbf{H}_2$. The result can be assumed as a complex value consisting of real constants a and b and with also

$$K(-j\omega) = \overline{K}(j\omega) \tag{25}$$

Substituting $K = a + jb$ into eq. (24) yields

$$\mathbf{H}_{\hat{p}\hat{g}}(j\omega) = \mathbf{H}_2\left\{(a-b+1)+j(a+b-1)\right\}/2 = \mathbf{H}_2 W_\omega$$
$$\text{where } |W_\omega| = \sqrt{A_\omega} \text{ and } A_\omega = (a-b+1)^2 + (a+b-1)^2 \tag{26}$$

From eq. (26), it is confirmed that the directional FRF can be expressed as the product of $\mathbf{H}_2$ and W_ω and the magnitude of W_ω is represented by $\sqrt{A_\omega}$. In other words, it is concluded that the magnitude of $\mathbf{H}_{\hat{p}\hat{g}}$ at the positive frequency can be expressed by the product of the magnitude of $\mathbf{H}_2$ and $\sqrt{A_\omega}$. The magnitude of $\mathbf{H}_{\hat{p}\hat{g}}$ at the negative frequency is

$$\mathbf{H}_{\hat{p}\hat{g}}(-j\omega) = \overline{\mathbf{H}}_2\left\{\overline{K}(1+j)+(1-j)\right\}/2 \tag{27}$$

It can be expressed as in eq. (27) in which $\mathbf{H}_2$ and K are represented by the complex conjugate of the positive frequency results of those in the negative frequency. Substituting the conjugate of K into the equation yields

$$\mathbf{H}_{\hat{p}\hat{g}}(-j\omega) = \overline{\mathbf{H}}_2 \left\{(a+b+1)+j(a-b-1)\right\}/2 = \overline{\mathbf{H}}_2 W_{-\omega}$$
$$\text{where} \quad |W_{-\omega}| = \sqrt{A_{-\omega}} \tag{28}$$

From eq. (28), the directional FRF at the negative frequency is represented as the product of $\overline{\mathbf{H}}_2$ and $W_{-\omega}$ and the magnitude of $W_{-\omega}$ is represented by $\sqrt{A_{-\omega}}$. From comparing eq. (26) and eq. (28), it follows that the magnitude of $\mathbf{H}_2$ and $\overline{\mathbf{H}}_2$ does not affect the magnitude of the directional FRF between the positive and the negative frequency since the relation of the conjugate gives the same magnitude. Therefore, the comparison can be achieved by the difference in magnitude of each *W* at the positive and the negative frequency.

$$A_{\omega} - A_{-\omega} = -8b \tag{29}$$

Eq. (29) shows that the magnitude of the directional FRF at the positive and the negative frequency is governed by the imaginary term of *K*. If the imaginary term has a negative value (i.e. $b<0$), then it can be concluded that

$$|\mathbf{H}_{\hat{p}\hat{g}}(j\omega)| > |\mathbf{H}_{\hat{p}\hat{g}}(-j\omega)| \tag{30}$$

The forward and backward waves of a rotating ring are represented by the negative and the positive frequencies [1, 14]. Therefore, if the imaginary value of the *K* satisfies the condition ($b<0$), it implies that the forward wave has a larger magnitude in the negative frequency region, while the backward mode has a larger magnitude in the positive frequency region. This fact is used to estimate the directivity of each wave with directional FRFs. The FRFs for radial direction in eq. (20) are re-expressed for a deeper understanding of *K*.

$$\mathbf{H}_{rr}(j\omega) = \sum_{n=1}^{N}\sum_{i=F,B}\left\{\frac{e^{jn(\theta_s-\theta_f)}\varphi_n\psi_n^H}{(j\omega - \lambda_n)} + \frac{e^{-jn(\theta_s-\theta_f)}\overline{\varphi}_n\psi_n^T}{(j\omega - \overline{\lambda}_n)}\right\}^i = \sum_{n=1}^{N}\sum_{i=F,B}\left\{\frac{Qe^{jn(\theta_s-\theta_f+\theta_n)}}{(j\omega - \lambda_n)} + \frac{Qe^{-jn(\theta_s-\theta_f+\theta_n)}}{(j\omega - \overline{\lambda}_n)}\right\}^i$$
$$= \sum_{n=1}^{N}\sum_{i=F,B}\left\{\frac{Qe^{jn(\theta_s-\theta_f+\theta_n)}\left(j\omega - \left(\overline{\sigma_n + j\omega_n}\right)\right) + Qe^{-jn(\theta_s-\theta_f+\theta_n)}\left(j\omega - (\sigma_n + j\omega_n)\right)}{\left(j\omega - (\sigma_n + j\omega_n)\right)\left(j\omega - \left(\overline{\sigma_n + j\omega_n}\right)\right)}\right\}^i$$
$$\text{where} \quad \varphi_n\psi_n^H = Qe^{jn\theta_n} \text{ and } \lambda_n = \sigma_n + j\omega_n \tag{31}$$

Eq. (31) is the representation which is replaced from the eq. (20) expressed by two numbers of first order basis to one number of second order basis and the mode shape information is also replaced with the Euler's form represented by combination of amplitude *Q* and phase $n\Theta_n$ from the product of φ_n and

Ψ_n^H. The eigenvalue of a rotating ring λ_n is represented by the combination of a real value σ_n and an imaginary value ω_n, where the real value stands for the energy dissipation and the imaginary value stands for the resonance frequency. Expressing K at a resonance frequency (ω_n) using eq. (31) yields

$$\begin{aligned} K(j\omega_n) &\cong \left\{ \frac{e^{jn(\theta_1-\theta_f+\theta_n)}\left(j\omega_n - \left(\overline{\sigma_n + j\omega_n}\right)\right) + e^{-jn(\theta_1-\theta_f+\theta_n)}\left(j\omega_n - \left(\sigma_n + j\omega_n\right)\right)}{e^{jn(\theta_2-\theta_f+\theta_n)}\left(j\omega_n - \left(\overline{\sigma_n + j\omega_n}\right)\right) + e^{-jn(\theta_2-\theta_f+\theta_n)}\left(j\omega_n - \left(\sigma_n + j\omega_n\right)\right)} \right\} \\ &\cong \left\{ \frac{e^{j2n(\theta_1-\theta_f+\theta_n)}\left(-\sigma_n + j2\omega_n\right) - \sigma_n}{e^{j2n(\theta_2-\theta_f+\theta_n)}\left(-\sigma_n + j2\omega_n\right) - \sigma_n} \right\} = \left\{ \frac{\alpha_n e^{j2n(\theta_1-\theta_f+\theta_n+\beta_n)} - \sigma_n}{\alpha_n e^{j2n(\theta_2-\theta_f+\theta_n+\beta_n)} - \sigma_n} \right\} \\ &\cong \left\{ \frac{\alpha_n e^{j2n\theta_1'} - \sigma_n}{\alpha_n e^{j2n\theta_2'} - \sigma_n} \right\} \end{aligned} \quad (32)$$

where $\alpha_n e^{j2n\beta_n} = -\sigma_n + j2\omega_n$

Eq. (32) shows the ratio of FRFs at two locations, which results into the ratio of the residues of each mode, assuming that each mode is well separated from each other, which is the case at the resonance frequencies. Representing the result in a trigonometric form to identify the imaginary value yields

$$\begin{aligned} K(j\omega_n) &\cong \left\{ \frac{\alpha_n e^{j2n\theta_1'} - \sigma_n}{\alpha_n e^{j2n\theta_2'} - \sigma_n} \right\} = \left\{ \frac{\alpha_n\left(\cos\left(2n\theta_1'\right) + j\sin\left(2n\theta_1'\right)\right) - \sigma_n}{\alpha_n\left(\cos\left(2n\theta_2'\right) + j\sin\left(2n\theta_2'\right)\right) - \sigma_n} \right\} \\ &\cong \left\{ \frac{\left(\alpha_n\cos\left(2n\theta_1'\right) - \sigma_n\right) + j\alpha_n\sin\left(2n\theta_1'\right)}{\left(\alpha_n\cos\left(2n\theta_2'\right) - \sigma_n\right) + j\alpha_n\sin\left(2n\theta_2'\right)} \right\} = \frac{A_1 + jB_1}{A_2 + jB_2} \\ &\cong \frac{\left(A_1A_2 + B_1B_2\right) + j\left(A_2B_1 - A_1B_2\right)}{A_2^2 + B_2^2} \end{aligned} \quad (33)$$

where $\theta_i' = \theta_i - \theta_f + \varphi_n + \beta_n,\ i = 1, 2$

Here, A and B represent the real and imaginary terms comprising the denominator and the numerator of K. Index i represents the measurement position 1 and 2. Considering only the imaginary term in eq. (33), the sign of the imaginary term is governed by the numerator since the denominator has always a positive value. This numerator of the imaginary part can be arranged by applying the trigonometric identity.

$$A_2B_1 - A_1B_2 = \alpha_n^2\sin\left(2n\left(\theta_1 - \theta_2\right)\right) - 2\sigma_n\alpha_n\sin\left(n\left(\theta_1 - \theta_2\right)\right)\cos\left(n\left(\theta_1' + \theta_2'\right)\right) \quad (34)$$

In the expression of eq. (34), it is expected that the magnitude of α_n^2 is much larger than $\sigma_n\alpha_n$ by eq. (32) (in the experimental results of a rotating tire, it is observed that the magnitude of α_n^2 is

normally ten times bigger than the magnitude of $\sigma_n \alpha_n$). Therefore, it can be assumed that the result of eq. (34) will be dominated by the first term of the equation. Under the assumption that the position of the second node is ahead of the first node (i.e. $\Theta_2 > \Theta_1$), the phase in the first term should be located at -180˚ ~ 0˚ to have a negative value, hence, the following relation can be established.

$$\theta_2 - \theta_1 < \frac{180°}{2n} \tag{35}$$

Eq. (35) shows that the locations of the two measurements can be decided based on the range of the interested mode number. For example, if one has interest up to 9th mode, the two locations should be located within 10˚. For the case of taking into account the second term of the equation, the result can be changed. The cosine part of the second term is assumed to have unit value (i.e. the maximum value of cosine) since the phase in the cosine cannot be estimated by experiments due to θ_1' and θ_2'. Then, the two measurement positions should satisfy the following relation to have a negative value of eq. (34) by considering the sine in the second term.

$$\theta_2 - \theta_1 < \frac{90°}{2n} \tag{36}$$

The relation in eq. (35) can be assumed as a necessary condition for applying the modified CMT technique and eq. (36) can be assumed as the sufficient condition. If eq. (36) is satisfied, the directional FRF $\mathbf{H}_{\hat{p}\hat{g}}(j\omega)$ shows larger value of the residue in the negative frequency for the forward wave and in the positive frequency for the backward wave. By using this fact, the directivity of each wave can be estimated. In a similar way as $\mathbf{H}_{\hat{p}\hat{g}}(j\omega)$, other directional FRFs can be identified of characteristics in the two sided frequency domain. Checking the results, $\mathbf{H}_{p\hat{g}}(j\omega)$ and $\mathbf{H}_{\hat{p}\hat{g}}(j\omega)$ show a similar trend to $\mathbf{H}_{\hat{p}\hat{g}}(j\omega)$, while $\mathbf{H}_{pg}(j\omega)$ and $\mathbf{H}_{p\hat{g}}(j\omega)$ show opposite trends to $\mathbf{H}_{\hat{p}\hat{g}}(j\omega)$. These results can be identified in the next section (simulation).

4 Simulation

In this section, the modified CMT technique introduced in the previous section will be verified by numerical simulation by the analytic formulae (eq. (20)). The ring model which is used in the simulation

is composed of 60 evenly distributed nodes from 0˚ to 360˚ with an increment of 6˚ and it rotates in counter clockwise direction with a speed of 8Hz. The applying force is located at the bottom of the ring in global coordinates (Fig. 2).

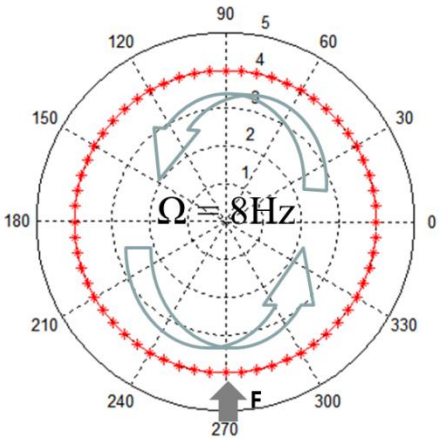

Fig. 2 Configuration of a rotating ring for simulation

In the simulation, the displacement response is obtained by eq. (18). The parameters used in eq. (9) are summarized in table 1. The simulation is conducted in two cases in terms of the location of measurement. In the first case, it is assumed that the measurements are located at 0˚(Θ_1) and 6˚(Θ_2). In the other case, the measurements are located at 0˚(Θ_1) and 30˚(Θ_2). The first case satisfies both conditions, while the second case does not satisfy both conditions imposed by eq. (35) and eq. (36) because the results are only identified up to the 7th mode for the both cases.

Table 1

Parameters for the ring model used in the presented simulation

Young's modulus	**$E = 4.76 \times e9$ N/m^2**
Density	**$\rho = 14500$kg/m^3**
Thickness	**$h = 14.1 \times e^{-3}$m**
Radius	**R = 0.3m**
Width	**b = 0.35m**
Damping ratio	**5%**

In the first simulation (for the case of 0˚ and 6˚), it is assumed that only the 3rd mode exists and the responses of the applied force are obtained at two positions. These two responses and one force are used to obtain the FRFs ($\mathbf{H}_1$ and $\mathbf{H}_2$) and the averaged result of the FRFs (Fig. 3 (a)). These data are also used to obtain directional FRFs (Fig. 3 (b)).

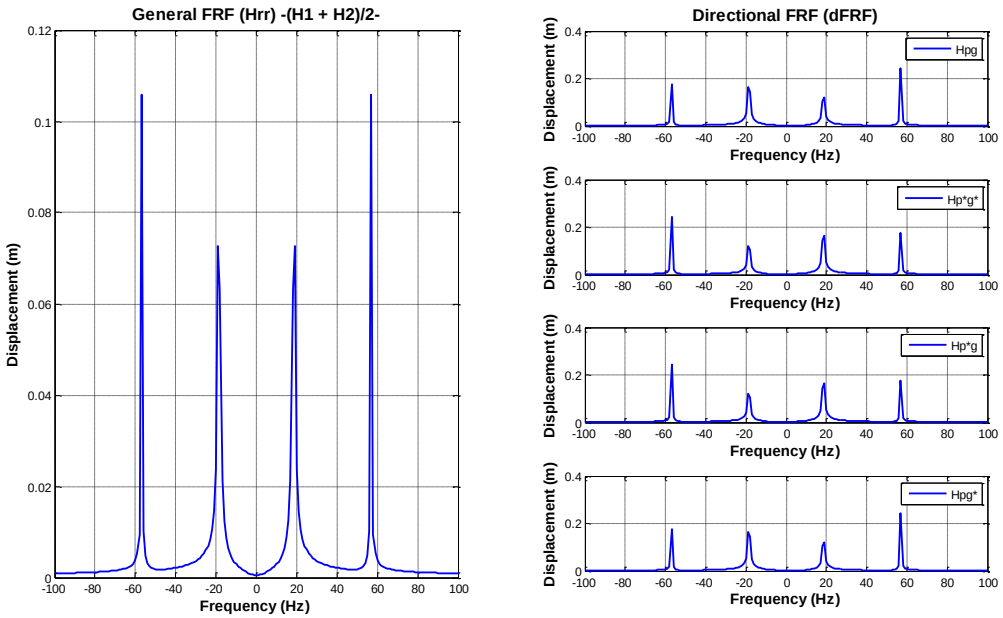

(a) (b)

Fig. 3 (a) Averaged FRF for 3rd mode at 0˚ (H_1) and 6˚ (H_2) (b) from top to bottom ($\mathbf{H}_{pg}(j\omega)$, $\mathbf{H}_{\hat{p}\hat{g}}(j\omega)$, $\mathbf{H}_{\hat{p}g}(j\omega)$ and $\mathbf{H}_{p\hat{g}}(j\omega)$)

The results of the resonance frequencies of the 3rd mode identified by eq. (12) are -56.91Hz for the forward wave and 18.53Hz for the backward wave. The general FRF cannot be used to estimate the directivity of each mode since it has identical magnitudes in the positive and the negative frequency regions as shown in Fig. 3 (a) (i.e. the magnitudes are 0.0727 at +18.53Hz and -18.53Hz and 0.1059 at +56.9Hz and -56.9Hz). Fig. 3 (b) shows the directional FRFs in the sequence of $\mathbf{H}_{pg}(j\omega)$, $\mathbf{H}_{\hat{p}\hat{g}}(j\omega)$, $\mathbf{H}_{\hat{p}g}(j\omega)$ and $\mathbf{H}_{p\hat{g}}(j\omega)$ going from top to bottom. As predicted in the previous section, it is observed in the second plot ($\mathbf{H}_{\hat{p}\hat{g}}(j\omega)$) that the peak at the forward wave resonance frequency (-56.91Hz) shows larger magnitude (0.24) than the magnitude (0.175) at the positive frequency (56.91Hz)

peak, while the peak at the backward resonance frequency (18.53Hz) shows lager magnitude (0.165) than the magnitude (0.12) at the negative frequency (-18.53Hz) peak. It is also observed that the plot of $\mathbf{H}_{\hat{p}g}(j\omega)$ shows the same trends as $\mathbf{H}_{\hat{p}\hat{g}}(j\omega)$ but that the plots of $\mathbf{H}_{p\hat{g}}(j\omega)$ and $\mathbf{H}_{pg}(j\omega)$ show opposite trends to $\mathbf{H}_{\hat{p}\hat{g}}(j\omega)$. Through this figure, the predicted trends in the previous section are verified. Similar simulations as shown in the previous result ($\mathbf{H}_{\hat{p}\hat{g}}(j\omega)$ in Fig. 3 (b)) have been conducted for both conditions (0˚ to 6˚ and 0˚ to 30˚) but with varying the assumed mode from 4th to 7th to compare the variation of the results with respect to measurement positions (Fig. 4).

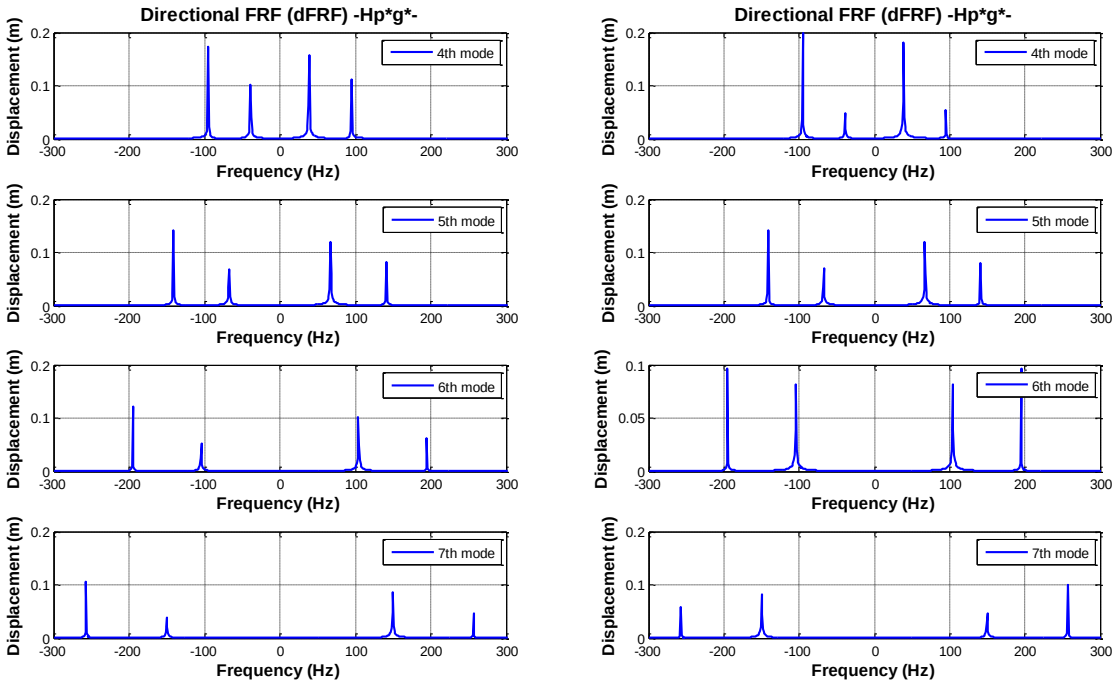

(a) (b)

Fig. 4 directional FRF simulation results ($\mathbf{H}_{\hat{p}\hat{g}}(j\omega)$) for 4th to 7th mode from top to bottom (a) measured at 0˚ (Θ_1) and 6˚ (Θ_2) (b) measured at 0˚ (Θ_1) and 30˚ (Θ_2)

The resonance frequencies (eq. (12)) -95.16 Hz, -141.14 Hz, -195.1 Hz and -257.1 Hz are for the forward waves and the frequencies 38.72 Hz, 67.34 Hz, 104.33 Hz and 149.64 Hz are for the backward waves. Based on these results, investigating the plots of the first simulation (Fig. 3 (b)), it shows that every forward wave has larger magnitude at negative frequency than the result in the positive region, while every backward wave always has a larger magnitude result at the positive frequency. For the

second simulation case (Fig. 4 (b)), however, the same conclusions as drawn from Fig. 4 (a) are concluded for the 4th and 5th mode, but for the 6th mode it shows similar magnitude results in both frequency regions and for the 7th mode the larger value appears in the negative frequency region for the backward wave and in the positive frequency region for the forward wave. From these results, it can be concluded that the range of the estimated mode number by the directional FRF is restricted by the interval of two measurement positions (verification of eq. (35) and eq. (36)).

5 Experiments

In order to validate the modified CMT introduced in this study, 45 locations on a rolling tire are measured, excited by a broadband excitation. Two of these 45 measurement locations are selected to apply the technique and the obtained results are compared to the results which are obtained by determining the mode shapes from all the measurements at all 45 nodes.

5.1 Experimental configuration for a rolling tire

The tire rolls on a steel drum and is excited by a metal strip (so-called cleat) which is fixed to the drum surface. A Laser Doppler Vibrometer (LDV) is used to measure the vibration velocity in the radial direction. As shown in Fig. 5, an array of 45 mirrors is used to direct the laser beam in the radial direction towards the tire surface.

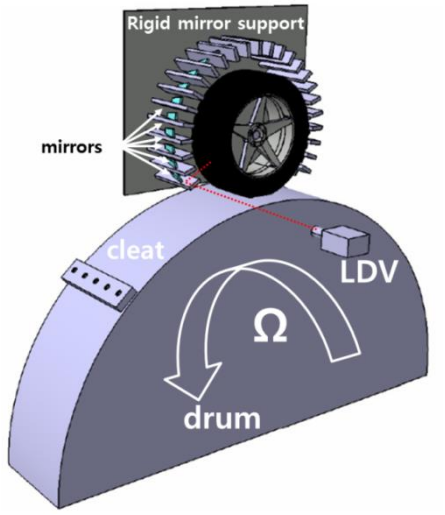

Fig. 5. Configuration for the vibration measurement of a rolling tire.

Since points close to the tire footprint are not accessible, the measurements start at about 48˚ clockwise (at 222˚) from the footprint/cleat contact (reference at 270˚) and end at 48˚ counter-clockwise (at 318˚) from the reference. The 45 measurement positions are evenly distributed every 6 ˚ from the start point and the measurement direction is clockwise. The response at each fixed location has been measured for 10 seconds. The number of cleat excitations and revolutions of the tire during this time period are determined by the rotational speed of the tire. Tachometers are used to count the number of cleat excitations (i.e. the number of revolutions of the drum) and the number of revolutions of the tire during 10 seconds. The time response due to every cleat passage is used in a time averaging process. At higher rotation speeds, the number of averages increases. However, the duration of the time response decreases since the time between two consecutive cleat passages become smaller. This causes a poorer resolution in the frequency domain. The tire spindle force signal is used to synchronize the vibration response at different points along the tire circumference. The excitation force at the tire footprint due to rolling over the cleat is not known. The measurement conditions are listed in table 2.

Table 2
Measurement conditions for the rolling tire

Measurement conditions	
Tire rolling speed [km/h]	100
Tire dimensions	205/55 R16
Inflation Pressure [bar]	2.2
Load [N]	7000
Applied Excitation	3x25 mm cleat
Sampling Frequency [kHz]	64

Fig. 6 shows the results of the measurement. Fig. 6 (a) shows the measured results of four quantities (tire vibration velocity, vertical spindle force, drum tachometer and tire tachometer) at fixed point 34. All results shown are normalized by the maximum value of each quantity. Fig. 6 (b) shows the averaged velocity calculated out of the response of 41 cleat passages. The duration of a single drum revolution is estimated to be 0.213 seconds. Fig. 6 (c) shows all averaged and synchronized velocity results and (d) shows all averaged and synchronized force results.

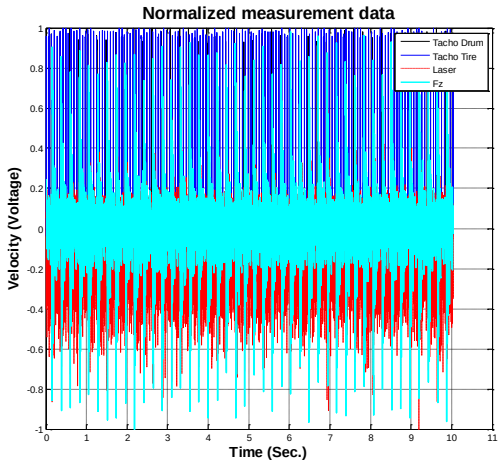

(a)

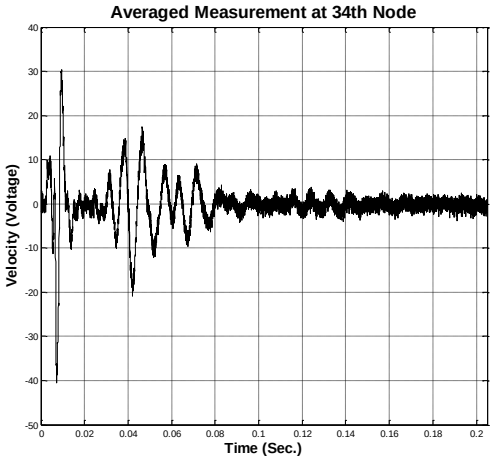

(b)

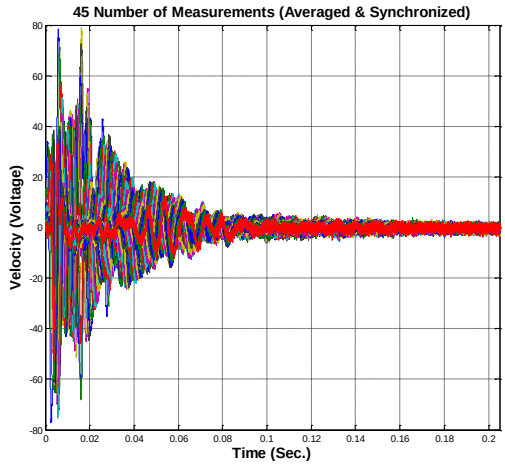

(c)

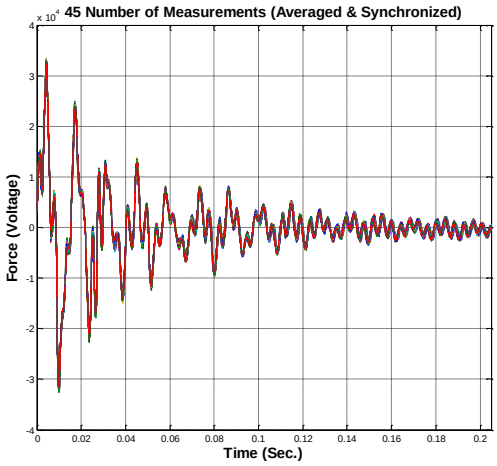

(d)

Fig. 6 Example of measurement data (a) 4 measured quantities (Tacho drum, tacho tire, laser and spindle force) at fixed point 34, (b) averaged velocity measurement at fixed point 34 over 10 seconds, (c) all 45 averaged and synchronized velocity responses, (d) all 45 averaged and synchronized vertical spindle force measurements.

Comparing the spindle force results of the 45 measurements indicate that the cleat excitation has a good repeatability and test conditions stay constant during the measurement of the vibration response at the different fixed points. In addition, the comparison also shows that the different responses are well synchronized. The frequency of the main spindle force oscillation corresponds to the first vertical tire resonance frequency [2]. The frequency contents of the vibration velocity at different points are found to be different from each other. All tire resonances have a different contribution to the total response in

different points. From these 45 results which are obtained by post processing, the dynamic characteristics of the tire can be analysed from the 45 averaged and synchronized responses.

5.2 Results

For the rolling tire, the excitation force as a result of rolling over the cleat is not known. Therefore, a general modal analysis method, which uses frequency response function, cannot be applied. Instead, an Operational Modal Analysis (OMA) method should be applied which only requires responses to estimate the modal parameters of the structure. Fig. 7 shows the measured power spectrum (solid line) of the vibration velocity for a tire rolling at 100km/h. The modal parameters of the rolling tire are estimated by using only response power spectra since the applied excitation force cannot be measured. The excitation force due to rolling over the 3x25 mm cleat has a relatively flat excitation spectrum. The PolyMAX modal parameter estimation method [15, 16] is applied to the power spectra of the responses because the frequency response functions of the rotating system have a similar form (eq. 20) as compared to the stationary system. Thus, the estimated modal parameters can be used to reconstruct the frequency response. Fig. 7 shows a good agreement between the measured and estimated power spectra. This agreement proves that the estimated modal parameter has fully described the measured dynamic behaviour. All estimated modal parameters (resonance frequency, damping and mode shape) are shown in Fig. 8.

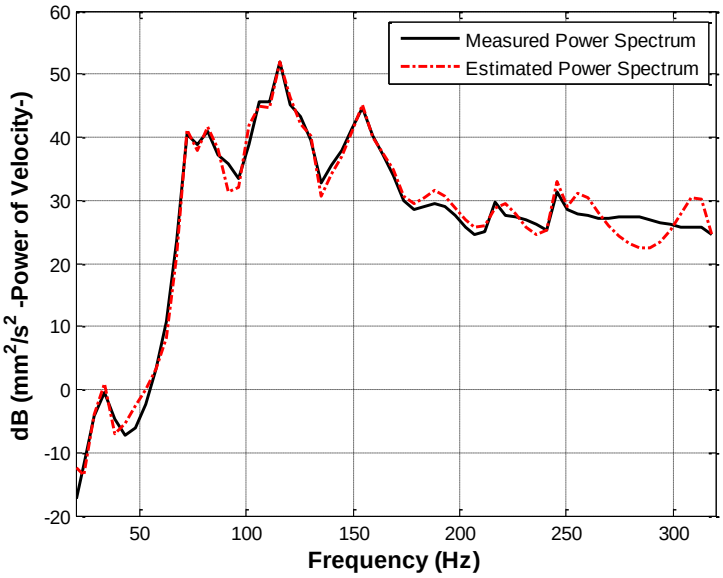

Fig. 7 Measurement (solid line) and estimated results (dotted line); Response power spectrum and its estimation of a rolling tire (100 km/h)

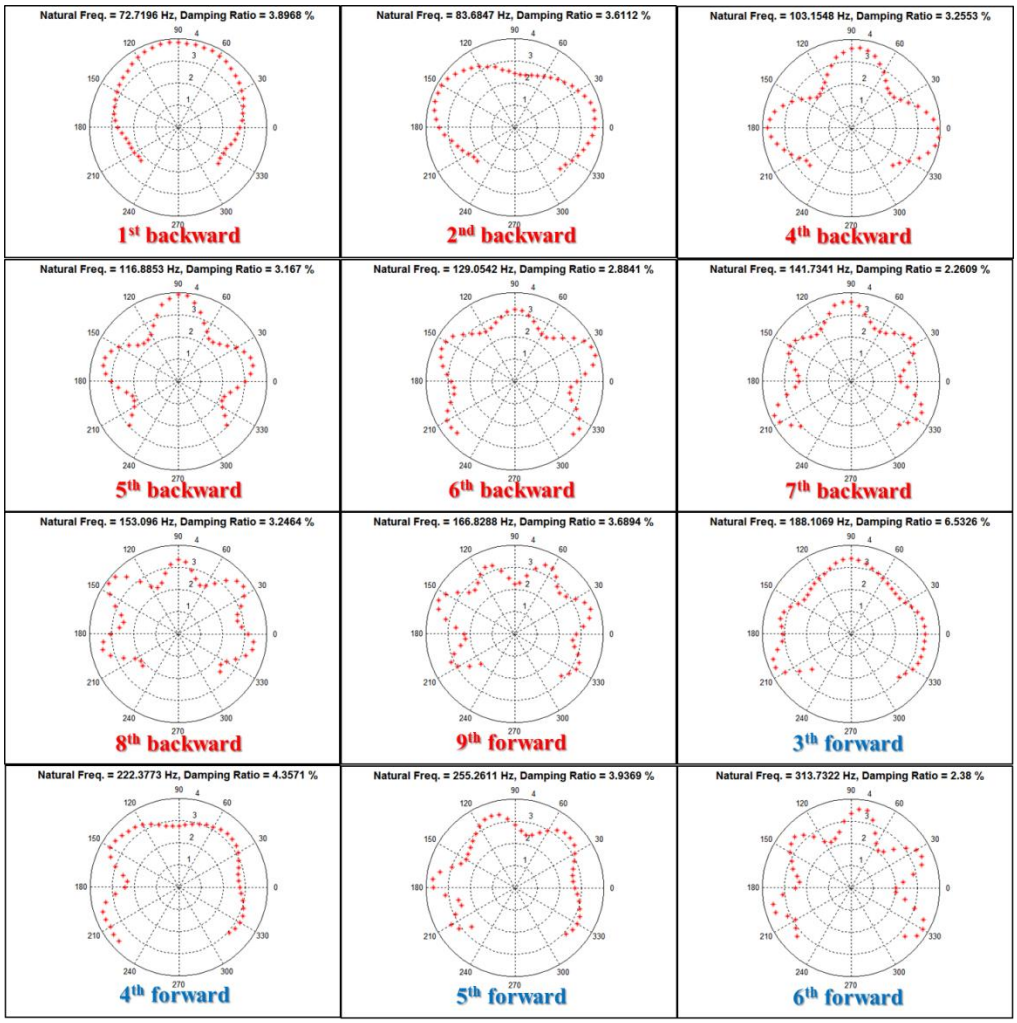

Fig. 8 Mode shapes for the rolling tire at 100km/h.

From Fig. 8, it is confirmed that several modes are not observed because the frequency content of the excitation force is dependent on the rotation speed and the cleat geometry for a rolling tire [1, 17]. More modes at higher frequencies will be identified when the rolling speed increases. This indicates that the excitation force levels at higher frequencies are higher as the rolling speed increases. As shown in Fig. 8, up to the 9th mode has been observed in the experimental results. Therefore, the satisfying location interval between two sensor positions in eq. (36) is less than 10˚. Any two nodes can be selected in this regard, so here two cases are considered, one is the 34th node (Θ_1 = 54˚) and 33th node (Θ_2 = 60˚) and another one is 19th node (Θ_1 = 144˚) and 18th node (Θ_2 = 150˚), among the nodes satisfying this condition are selected to obtain the directional FRF. The applied force f_r is assumed as an impulse force. The obtained directional FRF ($\mathbf{H}_{\hat{p}\hat{g}}$) is shown in Fig. 9.

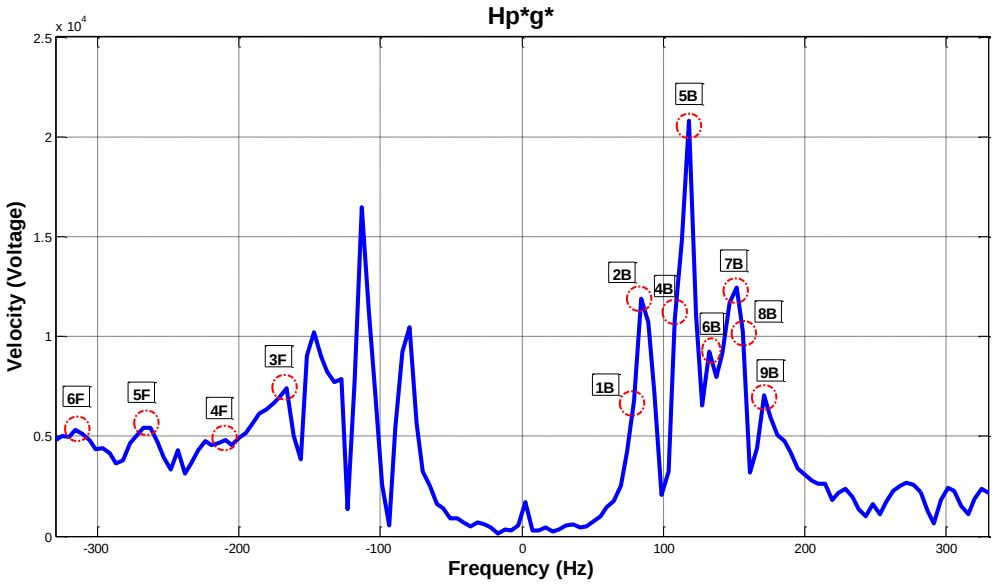

(a)

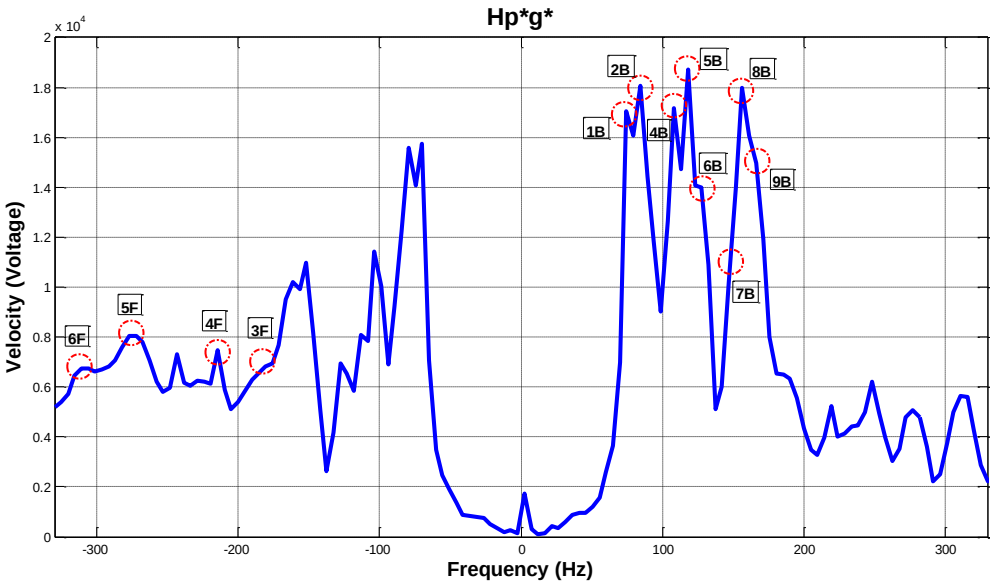

(b)

Fig. 9 directional FRF ($\mathbf{H}_{\hat{p}\hat{g}}$) results of a rolling tire (a) measured at 54˚ (Θ_1) and 60˚ (Θ_2) (b) measured at 144˚ (Θ_1) and 150˚ (Θ_2)

As shown in Fig. 9 (a), it is observed that for the frequency ranging from -200Hz~200Hz, the most of magnitude has larger values in the positive frequency region, while, it shows the opposite results for higher frequency values (i.e. -330Hz~-200Hz and 200Hz~330Hz). This trend shown in Fig. 9 (a) is also shown in Fig. 9 (b), even though it has different magnitude. And all resonance frequencies for each directional wave shown in Fig. 8, which are estimated by PolyMAX, are also shown in Fig. 9 with wave number and directional information (e.g. F and B). All results shown in Fig. 8 (resonance frequency, damping and directivity of wave) are listed in table 3.

Table 3

100Km/h						
		PolyMAX (with 45measurments)	Modified CMT (with 2measurements)			
Mode Number	Wave direction	Freq. (Hz)/Damping (%)	Negative Fre. (Hz)	Estimated Residues	Positive Fre. (Hz)	Estimated Residues
1	1B	72.72 / 3.9	-75.94	1.477	75.38	6.49
	1F	*	*	*	*	*
2	2B	83.69 / 3.61	-85.41	2.66	78.57	11.23
	2F	*	*	*	*	*
3	3B	*	*	*	*	*
	3F	188.1 / 6.53	-183.57	0.156	185	0.0238
4	4B	103.15 / 3.26	-103.8227	2.47	107.2554	6.49
	4F	222.37 / 4.36	-232.6	0.099	219	0.074
5	5B	116.9 / 3.17	-112.95	3.41	117.9	6.28
	5F	255.26 / 3.936	-263.47	0.359	253.7	0.0951
6	6B	129 / 2.9	-127	1.2	130.6	6.92
	6F	313.73 / 2.38	-315.7	4.4749	312.3	0.3724
7	7B	141.73 / 2.26	-132.6	0.58	144	7.98
	7F	*	*	*	*	*
8	8B	153.1 / 3.25	-153	1.48	156	12.97
	8F	*	*	*	*	*
9	9B	166.83 / 3.69	-167.7	0.62	169.4	3.56
	9F	*	*	*	*	*

* indicates a non-identified mode

The estimated residues in the negative and positive frequencies are listed in table 3 with corresponding negative and positive resonance frequencies. There is a small difference between the results, in which one result is estimated by traditional modal estimation method (PolyMAX) and another one is estimated by the directional FRF. For the 5^{th} forward wave case, for instance, the resonance frequency indicated by the modified CMT technique is -263.47Hz, because the residue in the negative frequency is larger than the positive frequency, it has around 8Hz magnitude difference with the frequency result which is estimated by PolyMAX. PolyMAX used 45 measurements while the directional FRF used only 2 measurements to estimate each result. The difference in the number of averages results in small difference between two results. From this table, one can confirm that the results are exactly the same as those predicted in the previous section in that the magnitude of the residue has a larger value in the positive frequency for the backward waves (notified by B in the table) and the negative frequency for the forward waves (F). From this fact it can be concluded that the modified CMT technique makes it possible to estimate the directivity of each wave.

6 Conclusion

There are two different directional waves in the rotating systems due to the Coriolis effect. Generally, directional waves are examined by using mode shapes which are obtained from measurements on a large number of positions. The complex modal testing technique, however, can give the directional information with only two position measurements. In this research, theoretically and experimentally, the difficulties of applying the complex modal testing to rolling tire analysis are introduced. In order to apply the technique with confidence, two conditions which should be satisfied in the experiment are introduced and these are explained and verified by simulations. In addition, the technique is applied to experimental measurements where by using only 2 measurement points, the same conclusions are obtained as in using a full data set of 45 measurement points.

7 Acknowledgement

The authors would like to thank the EU Seventh Framework Program (FP7/2010) for its support under the TIRE-DYN project (grant agreement no 251211). The first author received financing support from Dasan project and LMS International for the research stay in Leuven. He also thanks prof. Chong-Won Lee gratefully for his technical advice in this research. And this work was partially supported by a National Research Foundation of Korea (NRF) grant funded by the Korean government (2014R1A2A1A01005264).

Reference

[1] P. Kindt, Structure-borne tyre/road noise due to road surface discontinuities, Ph.D. thesis, Leuven, 2009.

[2] P. Kindt, D. Berckmans, F. D. Coninck, P. Sas and W. Desmet, "Experimetnal analysis of the structure-borne tyre/road noise due to road discontinuistes," *Mechanical Systems and Signal Processing*, vol. 23, pp. 2557-2574, 2009.

[3] I. Lopez, R. E. Blom, N. B. Roozen and H. Nijmeijer, "Modelling vibrations on deformed rolling tyres - a modal approach," *Journal of Sound and Vibration,* vol. 307, pp. 481-494, 2007.

[4] Y. -J. Kim and J. S. Bolton, "Effects of rotation on the dynamics of a circuar cylindrical shell with application to tire vibration," *Journal of Sound and Vibration,* vol. 275, pp. 605-621, 2004.

[5] C.-W. Lee, "A complex modal testing theory for rotating machinery," *Mechanical Systems and Signal Processing,* vol. 5, no. (2), pp. 119-137, 1991.

[6] S. Gong, A study of In-Plane Dynamics of Tires, Ph.D. Thesis, TU Delft, 1993.

[7] L. Kung and W. Soedel, "Free vibration of a pneumatic tire-wheel unit using a ring on an elastic foundation and a finite element model," *Journal of Sound and Vibration,* vol. 107, no. 2, pp. 181 - 194, 1986.

[8] P. Kindt, P. Sas and W. Desmet, "Development and validation of a three-dimensional ring-based structural tyre model," *Journal of Sound and Vibration,* vol. 326, pp. 852-869, 2009.

[9] W. Soedel, Vibration of shells and plates, third edition, revised and expanded, New York: Marcel Dekker, Inc., 2004.

[10] D. J. Ewins, Modal Testing : Theory, Practice and Application, Second Edition ed., Research Studies Press Ltd., 2000.

[11] C. G. Díaz, S. Vercammen, J. Middelberg, P. Kindt, C. Thiry and J. Leyssens, "Numerical prediction of the dynamic behaviour of rolling tyres," in *ISMA2012*, Lueven.

[12] W. Heylen, S. Lammens and P. Sas, Modal Analysis Theory and Testing, K. U. Leuven - PMA, 1998.

[13] L. Hermans and H. V. d. Auweraer, "Modal testing and analysis of structures under operational conditions: Industrial applications," *Mechanical Systems and Signal Processing,* vol. 13, no. (2), pp. 193-216, 1999.

[14] P. Zegelaar, The dynamic response of tyres to brake torque variations and road undevennesses, Ph.D. Thesis, TU Delft, 1998.

[15] C.-W. Lee and Y.-D. Joh, "Theory of excitation methods and estimation of frequency response functions in complex modal testing of rotating machincery," *Mechanical Systems and Signal Processing*, vol. 7, no. 1, pp. 57-74, 1993.

[16] C.-W. Lee and C.-Y. Joh, "Development of the use of directional frequency response functions for the diagnosis of anisotropy and asymmetry in rotating machinery: theory," *Mechanical Systems and Signal Processing*, vol. 8, no. 6, pp. 665-678, 1994.

[17] J. Lee, S. Wang, P. Kindt, B. Pluymers and W. Desmet, "Damping analysis with respect to rolling speed by analytic solution of a flexible ring model and its frequency response function derivation by modal summation method," *Internation Journal of Applied Mechanics*, vol. 6, no. 5, 2014 DOI: 10.1142/S1758825114500549.